

Fabrication and test of a MEMS combustor and reciprocating device

Dae Hoon Lee¹, Dae Eun Park², Joon Bo Yoon², Sejin Kwon¹ and Euisik Yoon²

¹ Division of Aerospace Engineering, Korea Advanced Institute of Science & Technology, 373-1 Kusong-dong, Yusong-gu, Taejon 305-701, Korea

² Division of Electrical Engineering, Korea Advanced Institute of Science & Technology, 373-1 Kusong-dong, Yusong-gu, Taejon 305-701, Korea

E-mail: melody@cais.kaist.ac.kr

Received 5 June 2001, in final form 7 November 2001

Published 11 December 2001

Online at stacks.iop.org/JMM/12/26

Abstract

We propose the concept of a microelectromechanical system (MEMS) scale reciprocating device powered by burnt gas and we have fabricated its prototype to investigate the applicability of the concept in a microscale power generator. In this investigation, combustion in a microscale chamber was studied using thermodynamic principles to estimate theoretical power output. We have carried out an evaluation of relevant subsystems and fabrication processes to realize the heat engine in such a small scale for further development of similar devices. A variable depth microcombustion chamber was built in-house to test the combustion characteristics in a small volume. Measurements include pressure transition after ignition and high-speed flame visualization. Test conditions include combustion chamber depth around the flame quenching distance, below which combustion theory predicts no burning. By analyzing the measured data, the combustion efficiency and available work were obtained and used for the design of a reciprocating MEMS device. The results of the combustion measurements required that the chamber height be 1 mm or more for stable ignition and flame propagation. Based on these findings of the microcombustion experiment, we formulated a MEMS fabrication process and made a reciprocating device. The device has a combustion chamber with a volume of 1 mm³, and the cross section of the cylinder has a rectangular shape with a height of 1 mm and a width of 2 mm. Photosensitive glass was chosen as a structural material. A thick photoresist mold and electroplating were used for constructing the overall structure. A single stroke experiment with hydrogen as a fuel was recorded by a high-speed digital video camera showing piston displacement at reasonable speeds.

(Some figures in this article are in colour only in the electronic version)

Nomenclature

C	capacitance	T	temperature
H	heating value	U	internal energy
I	current	V	voltage
m	mole	W	work
Q	electric charge	Y	mass fraction
S	entropy	h	heating value
		<i>Subscripts</i>	
		c	across capacitor

e	across electrode
0	surrounding
	Greek
χ	mole fraction
ϕ	equivalence ratio
η	combustion efficiency

1. Introduction

Many useful microsystems that are being proposed and are under development are required to perform mechanical works. Micro air vehicles, microrobots and nanosatellites are examples of such systems. Although the power requirement of microsystems is substantially less than macroscale devices, the mobile microsystems listed above have stringent weight and packaging limitations on their power sources. Despite many advantages, batteries cannot deliver enough power for the extended operation of mobile microsystems. In general, the energy density of batteries is too low for use where mechanical power is needed.

On the other hand, the smallest existing engine that has its application in model aircrafts is still too bulky and unreliable for applications in microsystems. As a result, the lack of a suitable micro power plant is the biggest obstacle in bringing about mobile microsystems. In recent years, several research groups have started working on concepts of micro internal combustion engines of various types. Fu *et al* [1] have described the development procedure of a microelectromechanical system (MEMS) rotary engine and Mehra *et al* [2] tested a prototype MEMS turbine engine that was fabricated by wafer bonding and deep reactive ion etching (RIE). Sitzki *et al* [3] reported an experiment on a microscale excess enthalpy burner. The advantage of internal combustion engines derives from the high-energy density of the liquid fuels. The energy density of hydrocarbon liquid fuel is approximately 1000 times as high as that of batteries. Even if we take into account the low thermal efficiency caused by reducing the scale of the device, the power generation using a microcombustor is an attractive alternative [4]. However, past research on microcombustion power devices placed emphasis on the fabrication processes and performance verification of subsystems such as microbearings and compressors and overlooked the importance of the thermofluidic phenomena in the devices.

In this paper, a more systematic approach is taken to examine the feasibility of MEMS scale engines. In addition to the manufacturing methods and selection of materials, the combustion and thermal processes must be understood to estimate available energy and ultimately power. These phenomena should be fully understood to determine the low limit of the scales for the engine and its combustion chamber. Such an investigation can be most effectively carried out in a combustion device solely designed for experimental data acquisition rather than in actual engine configuration.

Existing theories and measurement data on combustion are not adequate for the investigation of the process in a device whose scale is comparable to the flame thickness. Traditionally combustion research has focused on macroscale phenomena, partly because the thermal efficiency of a heat engine tends to be proportional to the size of the

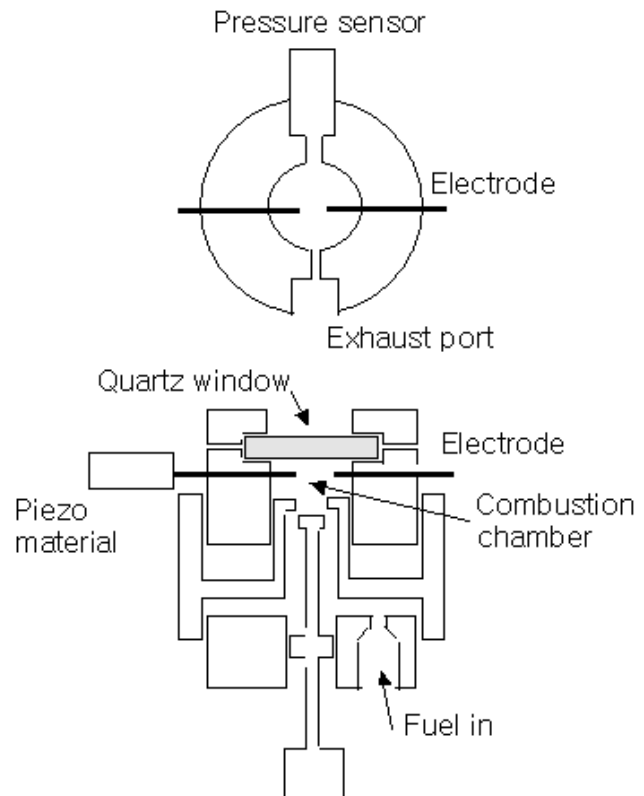


Figure 1. A schematic diagram of the variable depth combustor: upper and side views.

device. Reducing the scale of a combustor complicates the determination of design parameters of the device in a number of ways. Heterogeneous reaction on the wall that has been largely ignored in a macroscale reactor may become significant in microscale. As the ratio of heat generation to heat loss across the wall is inversely proportional to the length scale, a much higher level of heat loss is expected in a microcombustion chamber than in a macroscale device. If local heat loss is greater than combustion heat generated at that location, the flame quickly cools down and is extinguished.

The MEMS fabrication process and packaging requires that the chamber be laid out in a thin slab or layers of slabs bonded together with its height imposed by the flammability limit of the combustible gas mixtures. In order to allow an adequate gap between the walls, it is desirable to have a suitable fabrication process and a wafer material that can be engraved into a greater depth with accuracy. The ignition circuitry is integrated into the device and its design must take into account the means to acquire stable ignition with the least energy expenditure and with ease of fabrication. As the electrode gap and the combustor volume decrease, the required ignition energy first decreases then increases below certain scales [5].

2. Combustor experiment

2.1. Experimental setup and apparatus

To investigate issues related to combustion in a microscale confinement, a miniature combustion chamber was built by an in-house design as shown in figure 1. The combustor was made of acetal block by conventional machining to ensure both

Table 1. Quenching distance and minimum ignition energy of selected fuels.

	Quenching distance (mm)		Minimum ignition energy (10^{-5} J)	
	$\phi = 1.0$	Absolute	$\phi = 1.0$	Absolute
H ₂	0.64	0.61	2.0	1.8
CH ₄	2.5	2.0	33	29
C ₂ H ₄	1.3	–	9.6	–
C ₃ H ₈	2.0	1.8	30.5	26

Table 2. Test conditions (mm-psig).

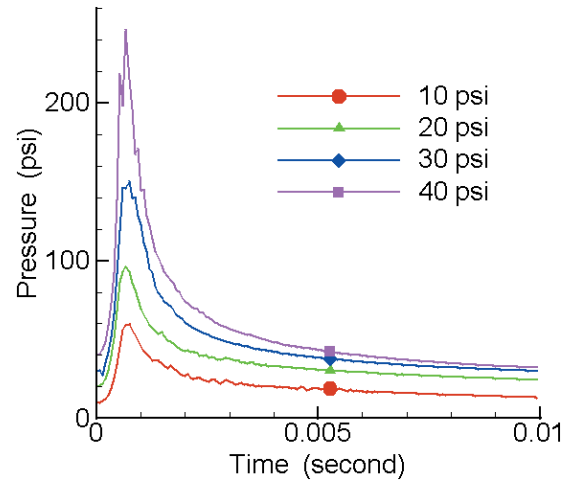
Height (mm)	Pressure (psig)			
	10	20	30	40
0.61	6.1	12.2	18.3	24.4
1.0	10	20	30	40
1.5	15	30	45	60
2.0	20	40	60	80
2.5	25	50	75	100
3.0	30	60	90	120

electric insulation for spark electrodes and ease of machining. The device had a cylindrical cavity with a diameter of 15 mm and an adjustable height from 0.4 to 4 mm to an accuracy of 14 μ m. The combustor was assembled from three separately made parts. A quartz glass window was mounted on top of the upper part allowing visual access into the chamber. The combustion chamber height was made adjustable to provide different test conditions of the chamber volume from 0.07 to 0.7 cc. Two ports were placed on the wall; one to accommodate the pressure transducer and the other to exhaust burnt gas.

Hydrogen and air were used for the combustible gas mixture. Hydrogen has an ignition energy, quenching distance and flammability region which are superior to those of other fuels. Table 1 [6] shows that typical hydrocarbon has a quenching distance of more than 1 mm and requires a larger combustor volume as a result. In all the measurements, the mixture ratio was fixed at a stoichiometric condition to guarantee a stable ignition and maximum heat release in a given volume. Fuel and air were mixed together in a surge whose pressure was regulated as specified by the test conditions and supplied to the combustor.

The test conditions are summarized in table 2 with the chamber height and initial pressure as control parameters. The chamber height was variable from 0.61 to 3 mm, while the initial pressure ranged from 10 to 40 psig. The lower limit of the chamber height approximately corresponds to the absolute quenching distance of the combustible mixture. At each test condition, at least ten realizations of pressure measurement and visualization were carried out. A piezoelectric pressure transducer mounted on the wall picked up the unsteady pressure variation following the ignition of the gas mixture. The pressure signal is passed to a PC at a sampling rate of 15–20 kHz. Flame propagation was also directly observed from the moment of ignition by a high-speed digital video camera at a framing rate of 13 500 frames per second (fps).

The ignition energy from a piezoelectric ignitor was evaluated from the voltage and current measurement across the electrodes. A piezoelectric switch converted mechanical energy into electrical spark discharge. The voltage across the

**Figure 2.** Typical pressure change for a 3 mm chamber depth at each initial pressure condition.

1.5 mm gap was about 5–7 kV with an instantaneous current of a few hundred amperes, when a spark was discharged. However, the accurate measurement of the current was difficult due to the extremely short duration of the discharge. The ignition energy supplied by the spark discharge can be calculated if the voltage and current data are given as follows:

$$E_i = \int VI dt \quad (1)$$

where E_i is the energy provided by the electrode, V is the voltage across the electrode and I is the current across the electrode.

If the current and voltage measurements involve uncertainties, an alternative method can be used. By inserting a capacitor into the ignition circuitry, the total discharge energy can be calculated from more slowly discharging capacitor voltage measurement [7]

$$\int V_e I dt = \int V_e \frac{dQ}{d\tau} dt = \int V_e C \frac{dV_c}{d\tau} dt \quad (2)$$

where V_e is the voltage across the electrode, V_c is the voltage across the capacitor, Q is the electric charge and C is the capacitance.

The spark energy was 1.7–1.8 mJ from either method. This value is sufficiently higher than the minimum ignition energy and warrants stable ignition.

2.2. Result

The measurement of pressure during flame propagation in a vessel displays the effect of the combustor scale on the thermodynamic process inside the chamber. Figure 1 shows the transient pressure after ignition in combustors with internal volumes of 0.35 and 425 cc. The smaller and larger combustors have surface area to volume ratios of 12.7 and 0.75 cm^{-1} , respectively. The peak pressure of a microcombustor is approximately half the peak pressure of a macroscale combustor. The scale effect was particularly noticeable during the phase of decreasing pressure after the peak pressure. The time of pressure decrease caused by cooling within a microcombustor was 1/100 of a macroscale combustor.

Figure 2 shows details of the pressure trace after ignition of the gas mixture. The results obtained with different initial

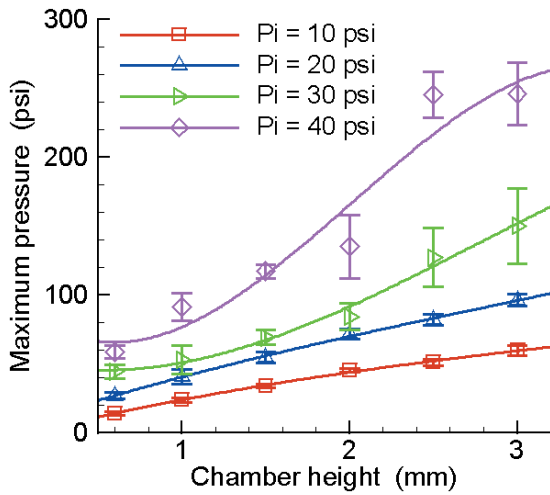


Figure 3. Maximum pressure obtained in all test cases.

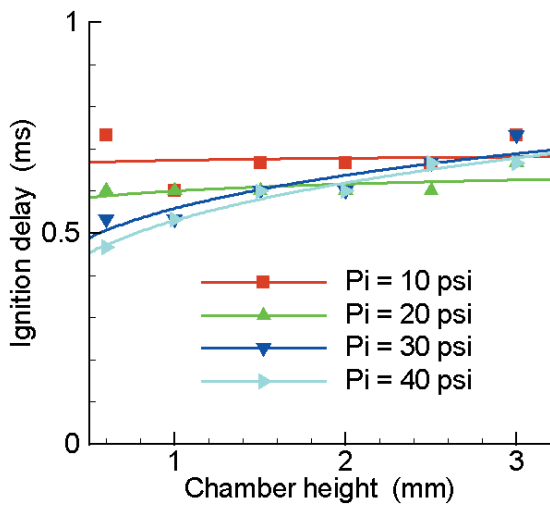


Figure 4. Time taken to reach maximum pressure from ignition.

pressures are plotted together. In this measurement, the chamber height was fixed at 3 mm. The pressure drop after the peak value is much faster than in a macrocombustor. In figure 3, the peak pressures of different test conditions are plotted together. Interestingly, even for the chamber height of 0.61 mm, which is slightly less than the quenching distance of stoichiometrically premixed hydrogen–air, partial pressure build-up and flame propagation was observed. However, the flame propagation in this extreme case was incomplete. Upon ignition, the chamber pressure increases rapidly in all conditions. In figure 4, the time from ignition to a peak pressure is shown. The chamber height and initial pressure appear to have no influence on this time gap.

The effect of reduced chamber height on the heat loss has been analyzed by comparing peak pressures obtained at different chamber heights with the same amount of gas mass. The product of initial pressure and chamber height is a measure of the mass as the cross-sectional area of the chamber is held constant and used as a parameter for the gas mass in figure 5. The peak pressure increases linearly as the gas mass parameter increases up to 900 mm-psig. For the gas mass parameter of 900 mm-psig and

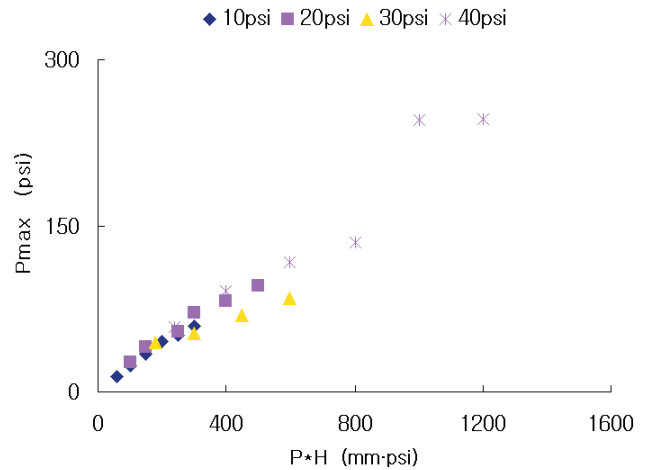


Figure 5. Peak pressure of test cases plotted in pressure–mass domain.

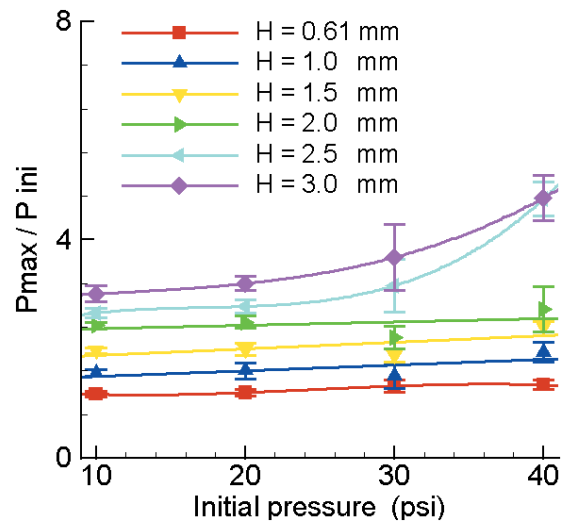


Figure 6. Peak to initial pressure ratio in each case.

below, the peak pressure is independent of chamber height. For the gas mass parameter higher than 900 mm-psig, we observed an adiabatic behavior which is found in macrocombustion. The ratios of peak pressure to initial pressure for all test conditions are presented in figure 6. This ratio represents the mean effective pressure of the burnt gas and is used to evaluate the available work. For chamber depths below 2 mm, the pressure ratio shows no dependence on initial pressure. When the chamber depth is beyond 2.5 mm, the ratio increases with increasing initial pressure, which is also observed in figure 5.

Another important parameter, which derives from the geometric configuration of the combustion chamber, is the surface to volume ratio. As the size of the combustion chamber decreases, the surface to volume ratio increases, resulting in more heat loss per unit volume of combustible gases. When this ratio is excessive, there is no detectable pressure rise after ignition. Hot gas generated by spark discharge quickly cools down and the rate of heat production by combustion is overwhelmed by heat loss to the wall and consequently quenching of the flame occurs. Figure 7 shows measured pressure ratios averaged over four realizations for each test condition. The vertical line is the limit beyond which the flame

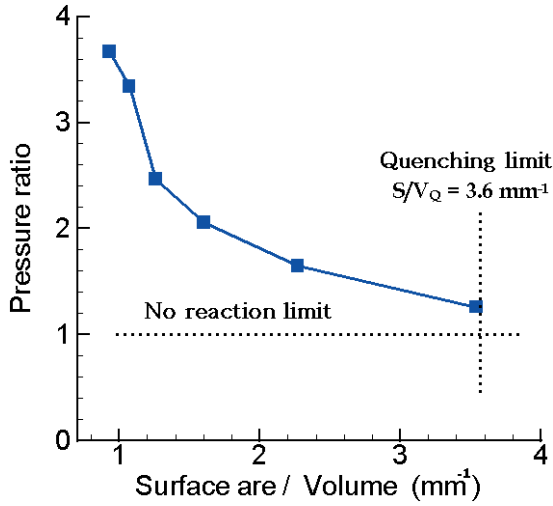


Figure 7. Pressure ratio in surface to volume ratio domain compared with quenching and no reaction conditions.

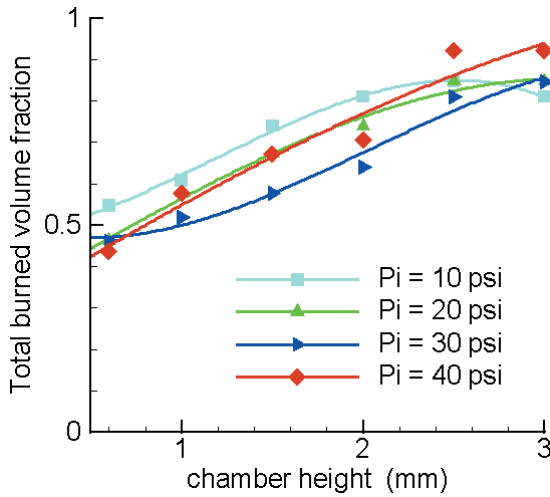


Figure 8. Total burned volume fraction at the time of quenching in each test case.

cannot sustain itself due to the aforementioned reasoning. The horizontal line is a limiting case of no pressure rise, i.e., no combustion. The pressure ratio curve crosses the vertical line before it falls on the horizontal line, by which we can conclude that the available work can be generated within the region between these two limiting conditions.

2.3. Analysis

Thermodynamic analysis has been carried out with the help of a theoretical model based on that of Lee and Kwon [8], which describes the modeling of the combustion process in a microcombustor. The model can predict the heat loss and quenching of the flame when the heat loss is excessive. The calculation involves finding the heat transfer coefficient from the measurements. The obtained total burned volume fraction is as shown in figure 8. Once the volume fraction of burned gas is known, the combustion efficiency and available work which the device can produce can be predicted.

The available work of the hot gas system is generated by the reaction while the system changes from state 1,

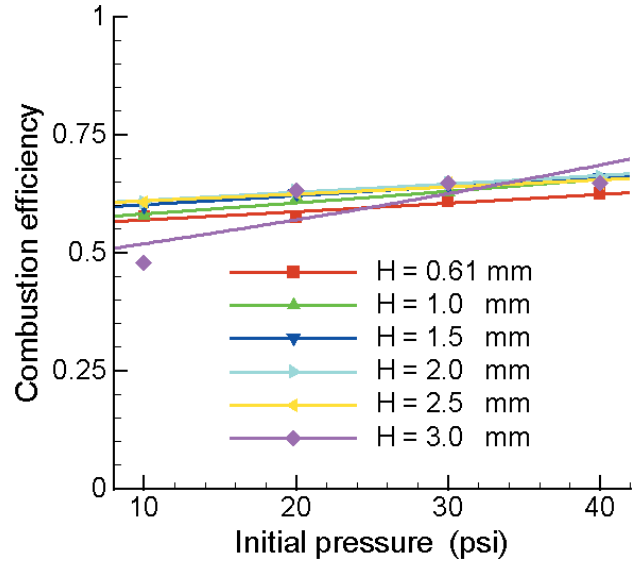


Figure 9. Combustion efficiency defined by the ratio of reversible work to ideal heat production in each test case.

before ignition, to state 2, where combustion stops either by quenching or complete burnout of the combustibles inside the chamber. Assuming the reversible process, the maximum work that can be released theoretically from the hot gas is expressed by [9]

$$W_{rev} = (U_1 - U_2) - T_0 (S_1 - S_2). \quad (3)$$

When the combustion is incomplete, the available work leads to

$$W_{rev} = (m_{eb}u_1 - m_{ib}u_2) + (m_{iu}u_1 - m_{iu}u_2) - T_0 \{(m_{eb}s_1 - m_{ib}s_2) + (m_{iu}s_1 - m_{iu}s_2)\} \quad (4)$$

where W_{rev} is the reversible work, T_0 is the surrounding temperature, m denotes mole, s is the entropy per unit mole and u is the internal energy per unit mole. The subscripts denote the following: e , after combustion; I , before combustion; u , unburned region; b , burned region.

The available work calculated from the measured data ranges from a few hundreds of millijoules for a chamber height of 1~2 mm to a few joules when the chamber height is 2.5 mm or more. The thermal efficiency ignoring various irreversibilities can be estimated by

$$\eta = \frac{W_{rev}}{h_{H_2} m_i \chi_{H_2}} \quad (5)$$

where η is the combustion efficiency, h_{H_2} is the heating value of hydrogen and χ_{H_2} is the mole fraction.

Figure 9 shows the combustion efficiency of the microcombustor. The combustion efficiency was approximately 0.6 for favorable test conditions. This value is roughly equivalent to those obtained by Waitz *et al* [10], but is much lower than the combustion efficiency of 0.9 or higher for a macroscale combustor. The overall thermal efficiency, which measures the effectiveness of a power plant, is obtained by the product of thermal efficiency and combustion efficiency. Considering relatively low efficiencies towards the lower limit

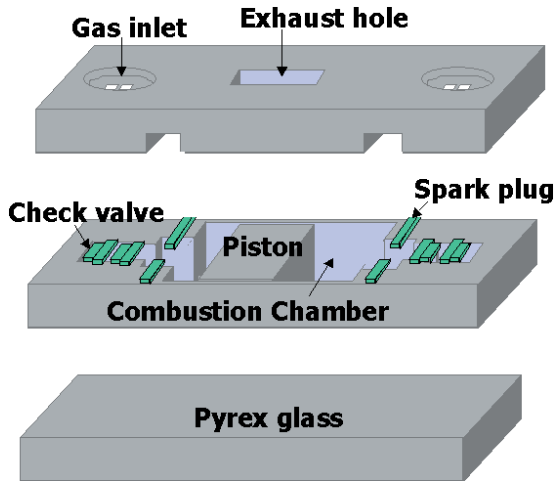


Figure 10. Schematic diagram of the MEMS reciprocating device structured by bonding three layers.

of the combustor height, 1~2 mm is a practical limit for the combustor height for the prototype fabrication of MEMS reciprocating device.

3. MEMS reciprocating device

3.1. Design

The experimental data obtained have been used in the design of a micro reciprocating device. In this section, we describe the design, fabrication process and actual combustion test of a prototype reciprocating device. The design concept tested here can be further developed and incorporated into a microengine system. The engine structure consisted of three wafer layers bonded together. A photosensitive glass wafer was used for the top layer where holes were made for the fuel intake and exhaust. The middle layer was also made of a photosensitive glass wafer and the cylinder and combustion chamber were engraved on this layer. The bottom layer was made of a Pyrex glass wafer and served as a base plate of the assembly. A schematic diagram of the device along with relevant dimensions is shown in figure 10. The current design has a combustion chamber depth of 1 mm, which is slightly greater than the quenching distance. The combustion data discussed in previous sections exclude chamber depths less than 1 mm and suggest depths of 2–3 mm for better combustion performance. However, a 1 mm design was chosen for the validation of the limiting scale and ease of fabrication (figure 11). In table 3, the wafer information is listed [11, 12]. The fabrication process is discussed in the following section.

3.2. Fabrication

For structures that have a high aspect ratio, a deep RIE process on a silicon wafer is commonly used. However, in this paper, the insulation of the spark electrode poses a problem with the silicon wafers. Without special insulation, it is very difficult to apply the high voltage required for spark discharge while using silicon wafers. The dielectric strength of a typical silicon dioxide layer is about 10^7 V cm⁻¹ and at least a 10 μm thick layer is needed for proper

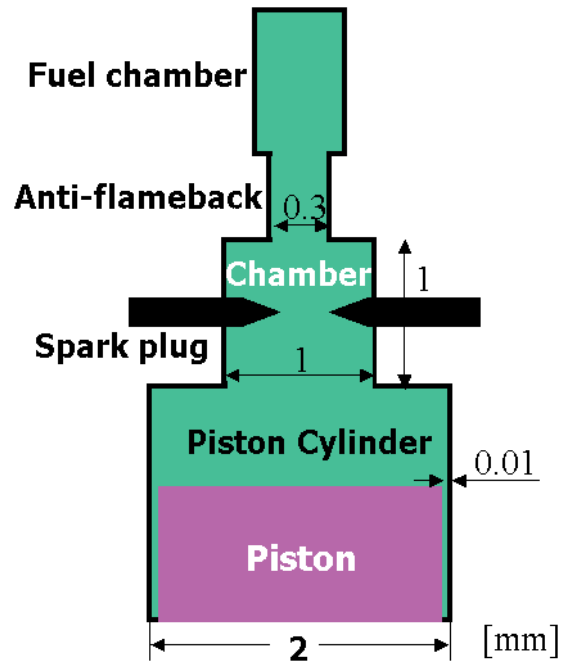


Figure 11. Detailed dimensions and shape of combustor part design.

Table 3. Wafer information.

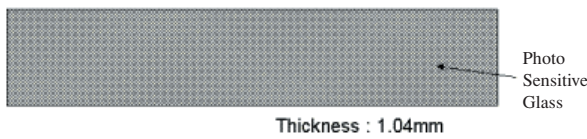
Mechanical properties	Glass	Ceramic
Young's modulus (N mm ⁻²)	78	88
Poisson's ratio	0.22	0.19
Density (g cm ⁻³)	2.37	2.41
Thermal properties		
Thermal expansion α_{20-300} (10 ⁻⁶ /K)	8.6	10.5
Thermal conductivity 20 °C (W/m · K)	1.35	2.73
Electrical properties		
Electrical conductivity 25 °C (Ω-cm)	8.1×10^{12}	5.6×10^{16}
Electrical conductivity 200 °C (Ω-cm)	1.3×10^7	4.3×10^7
Dielectric constant 1 MHz 20 °C	6.5	5.7

insulation. As an alternative, a photosensitive glass wafer was chosen as a structural material, since the electrical insulation and deep RIE process can be achieved easily with this material [13]. The ultraviolet (UV) exposed region of the photosensitive glass is crystallized after thermal treatment and can be etched anisotropically, resulting in accurate depth control.

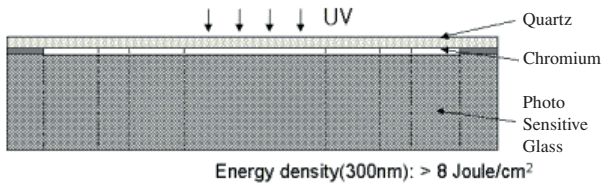
The fabrication process for each layer is described below, beginning with the middle layer. The photosensitive glass is exposed at UV light and thermally treated. The UV intensity was controlled at 8 J cm⁻². The wafer was then etched slightly to make a depth coverage that could be used as the align key. A Cr/Au seed layer was deposited for the electroplating process by thermal evaporator with the thickness of 250 Å/2500 Å. Thick photoresist (PR) (AZ9260) mold was formed on top of the wafer with a thickness of 45 μm. The PR patterning conditions are listed in table 4. A 40 μm deep Ni layer was electroplated on top of this with the process parameters shown in table 5. The UV exposed and thermally treated glass was etched in a hydrofluoric acid (HF) solution with 10% of HF

Chamber & Spark Plug

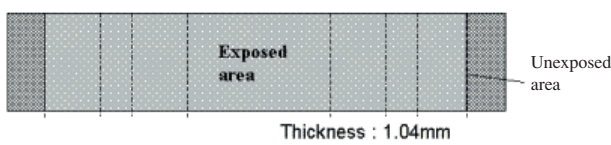
1. Starting Wafer (Foturan)



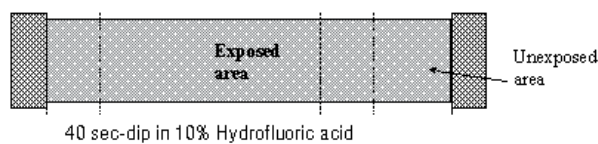
2. UV- Exposure (Photomask : Cr on Qtz.)



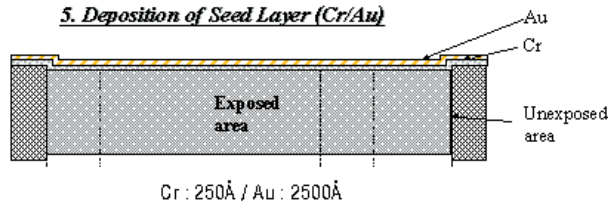
3. Heat Treatment



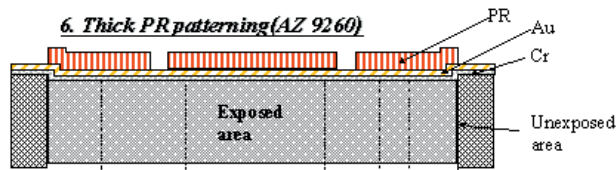
4. Shallow Etch of Exposed area



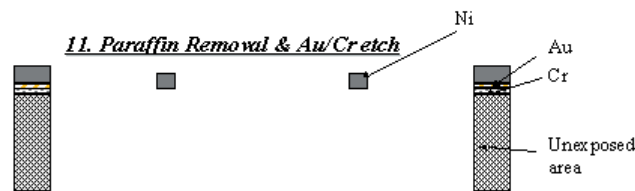
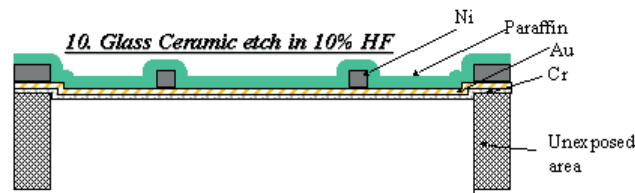
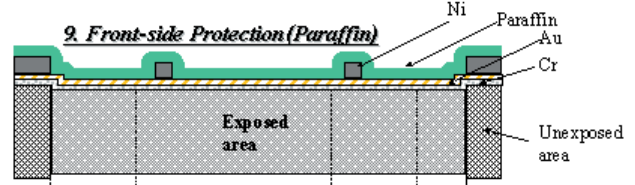
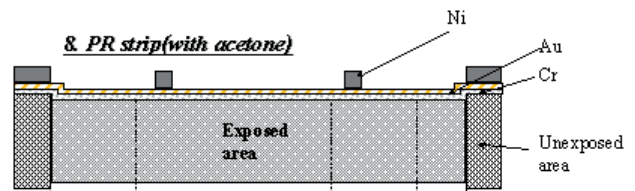
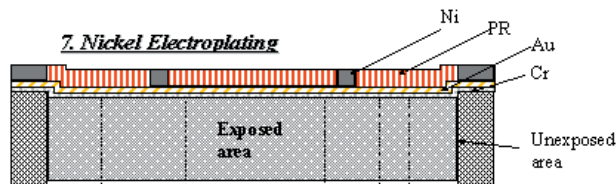
5. Deposition of Seed Layer (Cr/Au)



6. Thick PR patterning (AZ 9260)



7. Nickel Electroplating



Epoxy Bonding

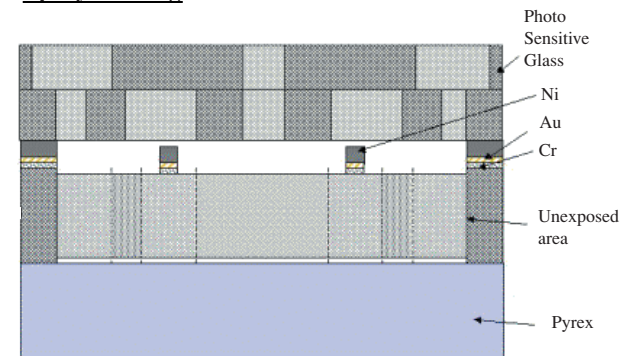


Figure 12. Fabrication process of the reciprocating device.

concentration by volume. To enhance the etching rate up to $20 \mu\text{m min}^{-1}$, we used an ultrasonic washing device for the process. The glass wafer was etched from the back to protect the seed layer and Ni structure during the etching process. For additional protection, the front was coated with a paraffin

layer. After the completion of the etching process, paraffin and AZ 9260 PR were stripped by boiling in trichloroethylene (TCE), acetone and methanol solutions in order.

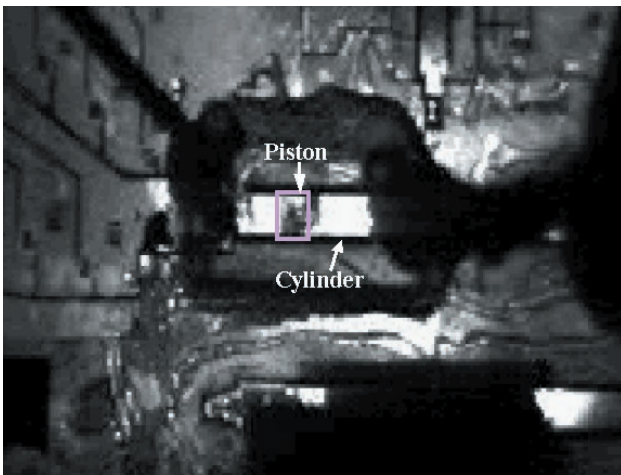
The same process was used for the top layer. However, the intensity of UV light was reduced to 3 J cm^{-2} , as the etching

Table 4. AZ9260 PR mold 45 μm thickness conditions.

PR coating	2000 rpm
Air stabilization	20 min
Soft bake (oven)	84 °C, 50 min
Soft bake (hot plate)	115 °C, 2 min
Air stabilization	60 min
UV exposure	3350 mJ cm ⁻²
DV 5:1	15–20 min

Table 5. Ni electroplating conditions.

pH	3.5~4.5
Temperature	40~60 °C
Current density	20 mA cm ⁻²
Plating rate	0.25 $\mu\text{m min}^{-1}$

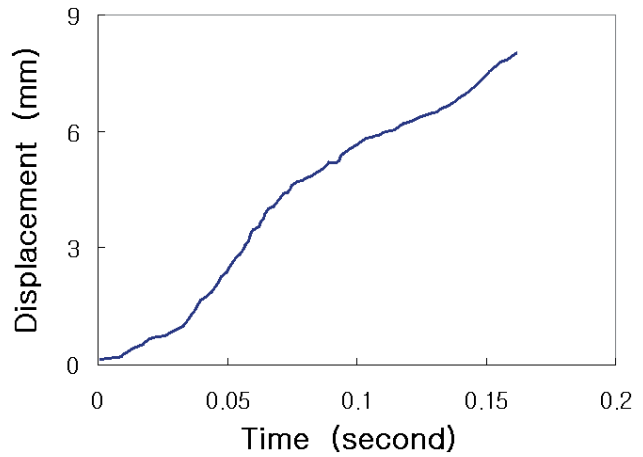
**Figure 13.** Images captured by video camera during the firing test of the device.

depth for the top layer is approximately half the thickness of the wafer. This is because the upper and lower halves are patterned differently.

The bottom and middle layers were bonded together and a piston was inserted into the cylinder. Lastly, the top layer was bonded to the middle layer by epoxy glue. The complete process is shown step-by-step in figure 12. This process is not complex but poses problems of gas leakage through a gap resulting from the epoxy bonding. Although not used in this paper, fusion bonding is expected to result in a better seal against gas leakage. Aside from the unsealed gap caused by bonding of different layers, there is also a gap between the side face of the piston and the cylinder wall. The gas leakage through these gaps undermines the performance of the heat device. For better construction, a better bonding method with lubricant on the sidewall of the cylinder can be considered.

3.3. Test result

To validate the reciprocating device, a hot test was carried out on the prototype fabricated with actual combustion. The test was recorded by a high-speed digital video camera at a framing rate of 9000 fps. Some of the captured images from these video tapes are given in figure 13. The images suggest

**Figure 14.** Piston movement trace captured by image tracing.

proper ignition and flame propagation within the cylinder. By analyzing the piston displacements of consecutive video images, piston velocity was derived. Figure 14 shows the displacement trace of the piston. The speed of the piston movement was relatively low, which was partly anticipated from the incomplete sealing of the cylinder. For quantitative diagnostics, monolithically implanted microsensors seem promising but have not been tried in this study.

4. Conclusion

A MEMS reciprocating device has been built and its operation has been shown. The design was based on data obtained from tests of a microcombustor. Simple pressure measurements and visualization of the test combustor have provided valuable information on the microcombustion process and the size limit of such devices for proper performance. When the combustion chamber had a height less than 2 mm, quenching and increased heat loss prohibited stable ignition and completion of combustion. The pressure drop following the peak pressure was rapid in microcombustion. A partial flame propagation and subsequent pressure rise were observed even in a combustor depth slightly less than the quenching distance. The time taken to reach peak pressure was independent of chamber height. Thermodynamic analysis of the measure pressure data found thermal energy release up to a few joules in a combustor height of 2 mm and more. The combustion efficiency was less than 0.7, which is lower than in a macroscale combustor. In order to achieve higher efficiency, additional measures such as preheating and/or insulation of the wall may prove effective.

Based on the findings of the microcombustion experiment, a MEMS reciprocating device was designed and a fabrication process was established accordingly. The fabrication process developed in this present study was simple and inexpensive but resulted in the leakage of hot gases through the gap in the bonded area. Photosensitive glass has been proven to be suitable for the reciprocating combustion device due to its favorable material properties, namely, high electric resistance, anisotropic etching characteristics and low thermal conductivity.

The combustion test of the reciprocating device has shown an active piston displacement. Although the test was plagued with the aforementioned leakage problems, it proved that such reciprocating devices can be built and enough theoretical power can be generated. The findings of this paper warrant further research on microcombustion phenomena and different concepts of microengines. In situations where further reduction of the combustion chamber is required, additional measures such as preheating the combustible gases and better insulation are needed. As for fabrication processes, a better bonding method between layers is desirable to eliminate gaps and gas leakage.

References

- [1] Fu K, Knobloch A J, Cooley B A, Walter D C, Fernandez-Pello C, Liepmann D and Miyasaka K 2001 Microscale combustion research for applications to MEMS rotary IC engine *NHTC 2001: Proc. Conf. ASME 35th National Heat Transfer* p 20089
- [2] Mehra A, Ayon A A, Waitz I A and Schmidt M A 1999 Microfabrication of high-temperature silicon devices using wafer bonding and deep reactive ion etching *IEEE J. MEMS* **8** 152
- [3] Sitzki L, Borer K, Wussow S, Schuster E, Maruta K and Ronney P D 2001 Combustion and power generation in microscale excess enthalpy burners *2nd Joint Meeting of the US Section of the Combustion Institute*
- [4] Epstein A H *et al* 1997 Power MEMS and microengines *Transducers97 (Chicago, 1997)* pp 753–6
- [5] Tohoku university 1968 Gas discharge (*Tohoku University Basic Electronics Lecture Series vol 4*)
- [6] Turns S R 1996 *An Introduction to Combustion* (New York: McGraw-Hill) p 236
- [7] Lessor D L, Herling D R, Sharma A K and Speck C 2000 Development of a non-thermal plasma reactor electrical model for optimum nox removal performance *SAE International Fall Fuels and Lubricants Meeting and Exposition (Baltimore, Maryland)*
- [8] Lee D H, Choi K H and Kwon S 2001 Measurement and modeling of combustion in a microcombustor *AIAA 2001: AIAA 36th Thermophysics Conf.* AIAA Paper: AIAA2001–3077
- [9] Cengel Y A and Boles M A 1989 *Thermodynamics—An Engineering Approach* 2nd ed
- [10] Waitz I A, Gauba G and Tzeng Y-S Combustors for micro-gap turbine engines 1998 *ASME J. Fluids Eng.* **120** 109
- [11] <http://www.mikroglas.com>
- [12] <http://www.design.Caltech.edu/micropropulsion/foturan.html>
- [13] Park D E 2001 Experimental fabrication of a microengine using micromachining technology *MS Thesis KAIST*